Quartz-enhanced Photoacoustic Spectroscopy for Trace Gas Sensing

Pietro Patimisco
University of Bari, Bari, Italy

Vincenzo Spagnolo
Politecnico of Bari, Bari, Italy

*Photoacoustic spectroscopy (PAS) was established itself over the last decades as a powerful detection technique, capable of measuring trace gas concentrations at part-per-billion level. The basic principles of laser PAS are provided with a discussion on photoinduced acoustic wave generation and its detection. Quartz-enhanced photoacoustic spectroscopy (QEPAS), where a quartz tuning fork (QTF) is used to detect acoustic waves, is presented in detail as an improvement of the conventional microphone-based PAS. QEPAS does not require an optical detector, requires extremely small volumes, laser wavelength independent, and immune to environmental noise. The discussion covers several aspects of QTF resonance properties, regarding flexural modes, dissipation processes, and quality factor (*Q*-factor). The main advantages achievable by exploiting custom QTFs for QEPAS sensing and novel approaches such as the excitation of overtone modes are highlighted and discussed. Finally, the most performant QEPAS sensors for real-world applications are reviewed. Environmental monitoring of* CH_4*, CO, and* N_2O *and a QEPAS sensor for leak detection in mechatronic systems as well as hydrocarbon detection in petrochemical industry are few examples of QEPAS sensors already tested in out-of-laboratory environments. The obtained results clearly demonstrate the potential of QEPAS-based sensors for in situ operations.*

1 INTRODUCTION

Gas detection has a great impact in a wide range of applications. For example, the use of high-sensitivity gas detectors is widespread in atmospheric science to measure and study the profile and pathways of different gas species, including greenhouse gases. Gas sensing finds applications also in life science and breath analysis: various potential biomarker gases are under study for use in human breath diagnostics. Quantitative detection of gases is traditionally performed by laboratory analytical equipment such as gas chromatographs and mass spectrometers or by small low-cost devices such as pellistors, semiconductor gas sensors, or electrochemical devices. Gas sensors based on optical absorption are a promising alternative that can offer fast responses times (usually below 1s), minimal drift, and high gas specificity, with zero cross-response to other gases. In addition, noninvasive measurements can be performed in real time and in situ. The absorption lines or bands are specific to each gas species, thus guaranteeing high selectivity of single gas species detection. In the near- and mid-infrared region (0.7–25 μm), roto–vibrational transitions occur. A molecule exhibits a certain number of vibrational modes, which are strictly connected to the molecule geometry and composition. The vibrations can involve localized groups of polyatomic molecule, such as stretching or bending of terminal groups, or can involve the vibration of a specific group. The latter one involve strong coupling between stretching and bending motions of atoms in a straight or branched chain or a ring. Such vibrations are called skeletal vibrations and are specific for a particular molecule. The spectral region between 6 and 25 μm, where skeletal vibrations fall, is often referred to as the fingerprint region, since many molecules, simple or complex, such as volatile organic compounds, exhibit characteristic absorption bands. All spectroscopic techniques are based on optical absorption, which are governed by Beer–Lambert's law that describes the attenuation of a monochromatic beam of intensity after passages through an absorbing species. Starting from this principle, gas sensing techniques based on measurement and analysis of optical absorptions at specific wavelengths have been developed. Considering that the highest detection sensitivity is most desirable, the choice of a specific

Encyclopedia of Analytical Chemistry, Online © 2006–2021 John Wiley & Sons, Ltd.

This article was published in the *Encyclopedia of Analytical Chemistry* in 2021 by John Wiley & Sons, Ltd.
DOI: 10.1002/9780470027318.a9760

technique is mainly determined by the final application requirements and constraints. Minimum detection limits (MDLs) are usually quantified as the noise equivalent concentration (NEC). The convention adopted is that the NEC is the gas target concentration giving a signal equal to the root-mean-squared value of signal intensity variations (1σ). Furthermore, it is also important to consider the available optical laser power, the strength of the selected absorption line, and the signal integration time used for the gas concentration measurements to quote limits in the units of normalized noise equivalent absorption coefficient (NNEA) measured in $\mathrm{cm^{-1}\,W\,Hz^{-1/2}}$, by normalizing the noise equivalent absorption to a 1-Hz measurement bandwidth. The optical sensors that have proved to be effective for trace gas detection can be divided into two major groups: direct and indirect absorption-based sensors. Direct absorption techniques use multipass cells or high-finesse optical cavities. In multipass cells, the laser beam experiences multiple reflections at different points on two large-diameter focusing mirrors. In this way, the optical pathlength can be as high as 100 m even if the gas cell length is on the order of tens of centimeters. The alignment is critical to preserve the pattern of laser beam reflections between the two mirrors of the cell. Indeed, the signals are strongly affected by fringe-like noise patterns when misalignments occur. In cavity-enhanced absorption spectroscopy, the gas cell is composed of a high-finesse optical cavity. Extremely long pathlength cells can be obtained by using mirrors with high reflectivity ($R > 99.99\%$), achievable by depositing dielectric coatings. The simplest resonant cavities are formed in the manner of a high-finesse Fabry–Perot etalon. The cavity-enhanced-based techniques suffer from misalignment since the linewidth and spectral purity of longitudinal cavity modes can be deteriorated by a nonoptimal matching between the laser beam path outside and the light propagation through the cavity itself.(1) The requirement of laser beams with high spatial quality as well as a narrow linewidth is mandatory. The cost that this kind of technique has to pay for a lower NNEA and higher sensitivity – down to part per quadrillion – is a significant increase in the optical pathlengths as well as in the overall size of the sensors. Both multipass cells and optical cavities must be combined with optical detectors and can work in a narrow bandwidth of laser emission wavelengths because of the mirror reflectivity dependence on the laser wavelength. Therefore, the use of a widely tunable laser sources for analyzing gas mixtures potentially containing many broadband absorbers is generally precluded. Spectroscopic techniques based on indirect absorption spectroscopy measure the effect of the optical absorption produced in a gas sample. Photoacoustic effects arise from the generation of acoustic waves due to the absorption of modulated light in the gas sample. The excitation and subsequent relaxation of the sample produce a local change in thermodynamic parameters (e.g. pressure, temperature, density), which can be detected accordingly. The modulated heat release produces a periodical temperature change, which in turn generates pressure waves with the same periodicity, namely, acoustic waves, which propagate with relatively low damping far from the heat source and can easily be detected by pressure transducers, such as capacitive microphones or QTFs. The exploiting of photoacoustic effect can result in a powerful tool for ultra-sensitive spectroscopic techniques. Theoretical models proposed by Slatkine(2) showed that NNEA as low as $10^{-11}\,\mathrm{W\,cm^{-1}\,Hz^{-1/2}}$ can be reached with continuous-wave (CW) modulated sources. These levels were experimentally achieved by Zharov and Letokhov,(3) Spagnolo et al.,(4) and Tomberg et al.(5) The experimental set-up for PAS is relatively simple: the laser beam is intensity modulated and focused into an acoustic cell containing the gas mixture. When the laser modulation frequency matches the resonance frequency of one of acoustic modes, a standing-wave vibrational pattern is created within the acoustic cell, which acts as an acoustic resonator. In other words, cell resonances enhance or amplify acoustic power at the resonance frequency. The degree of amplification or resonant quality of an acoustic cell is described by the Q-factor Q. Q-values of greater than 1000 have been reported, and values of a few hundred are typical for a radial resonance mode. Since acoustic waves have the same frequency as the laser modulation, a low-noise, phase-sensitive demodulation of the acquired signal is performed by a lock-in amplifier.

2 HISTORICAL OVERVIEW OF PHOTOACOUSTIC EFFECT

The photoacoustic effect was observed by Bell more than a century ago (1880) while he was working on the improvement of a photophone, in an accidental way. Bell realized that when a light beam is periodically 'interrupted' by a chopper and subsequently focused on a layer of thin material (a diaphragm in connection with an acoustic horn), a sound wave is produced. In addition, the generated acoustic signal increased its intensity when the layer exposed to the beam was dark in color. Thus, Bell realized that this effect was related to the absorption of light by the thin layer. The photoacoustic effect occurs in all kinds of materials (solids, liquids, and gases), and scientists began to study the phenomenon and its possible applications. However, due to the lack of appropriate equipment (such as light sources, microphones), the photoacoustic effect was completely forgotten for more than half a century. PAS was used by Viengerov(6) for the

Encyclopedia of Analytical Chemistry, Online © 2006–2021 John Wiley & Sons, Ltd.
This article is © 2021 John Wiley & Sons, Ltd.
This article was published in the *Encyclopedia of Analytical Chemistry* in 2021 by John Wiley & Sons, Ltd.
DOI: 10.1002/9780470027318.a9760

first spectroscopic gas analysis in 1938 to study infrared light absorption in gas mixtures. With the development of the laser in 1960, there was yet another revival in gas analysis. The high power achievable with laser technology allowed ultralow gas concentration detection and analysis. Other important advantages of the laser as a light source came from the high degree of spectral purity, high stability, and reproducibility. Kerr and Atwood(7) used for the first time a CW CO_2 laser as a radiation source to detect CO_2 in nitrogen. Kreuzer et al.(8) reported the detection of methane with an MDL of 10 parts per billion (ppb) using a HeNe laser as the light source. Trace gas detection with a PAS system was studied by Max and Rosengren(9) using a resonant acoustic gas cell, showing that the MDL of gas detection was determined by microphone and preamplifier noise. They showed that the acoustic noise detected by the microphone is the most important factor for the MDL. They employed a CO_2 laser as the light source for trace amounts of NH_3 in gas detection. With a laser power of 280 mW, they reached an MDL of 3 ppb. A detailed review on history of photoacoustic has been provided by Manohar and Razansky.(10) In the next section, the theoretical foundation is described for the photoacoustic effect. In addition to gas concentration analysis, the photoacoustic effect can be used for the investigation of vibrational relaxation rates and molecular energy transfer in gases.

3 THEORY OF THE PHOTOINDUCED ACOUSTIC WAVE GENERATION

The theoretical modeling of photothermal and photoacoustic generation has been extensively studied by several authors, such as Kreuzer(11) and Bialkowski et al.(12) The generation of the acoustic wave can be divided into three steps: (i) absorption of incident photons and subsequent excitation of the gas molecules; (ii) generation of thermal and acoustic waves; (iii) detection of the photoinduced effects through an acousto-electric transducer. In Figure 1, the main processes that take place in the production of thermal effects are sketched.

$N_0(\boldsymbol{r},t)$ and $N_1(\boldsymbol{r},t)$ are molecular density for the fundamental energy state E_0 and the excited energy state E_1, respectively, ρ_ν is the energy density of radiation, A_{10} and B_{10} are the Einstein coefficient for spontaneous emission and stimulated emission, respectively, and c_{10} is the nonradiative transfer rate via collisions. The rate equation for the population $N_1(\boldsymbol{r},t)$ can be expressed as

$$\frac{dN_1}{dt} = \rho_\nu B_{10}(N_0 - N_1) - (A_{10} + c_{10})N_1 \tag{1}$$

The inverse of lifetime τ of the excited state can be expressed as a sum of A_{10} and c_{10}, i.e. $1/\tau = A_{10} + c_{10}$, and in a weak optical absorption approximation, namely, $N_1 \ll N_0$ and N_0 time-independent, the previous equation can be rewritten as

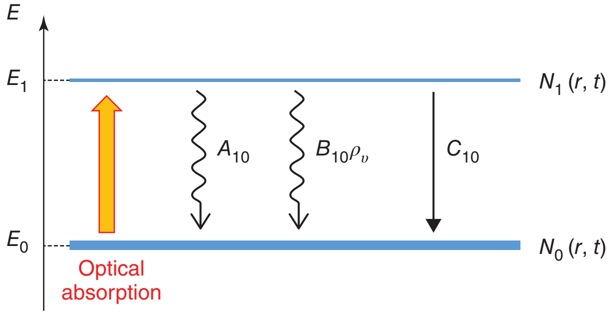

Figure 1 Two-level energy scheme.

$$\frac{dN_1}{dt} = \rho_\nu B_{10} N_0 - \frac{N_1}{\tau} \tag{2}$$

The term $\rho_\nu B_{10}$ represents the absorption optical rate and can be expressed as the product between the photon flux and absorption cross-section σ. When the photon flux is modulated at a frequency ω, it can be expressed as

$$F(\boldsymbol{r}, t) = F_0(\boldsymbol{r})(1 + \delta e^{i\omega t}) \tag{3}$$

When $\delta \ll 1$, a small-amplitude sinusoidal modulation is superimposed to a time-independent photon flux $F_0(\boldsymbol{r})$. By combining Equations (2) and (3), the differential equation can be solved, and the population density of the excited level can be related to the optical absorption of modulated light:

$$N_1(\boldsymbol{r}, t) = \frac{N_0 \sigma F_0(\boldsymbol{r}) \delta}{\sqrt{1 + \omega^2 \tau^2}} \tau e^{i(\omega\tau - \vartheta)} \tag{4}$$

where $\vartheta = arct(\omega t)$ is the phase difference between the modulation of the population density and the photon flux. Thus, the heat rate generated by the optical absorption can be related to the population density:

$$H(\boldsymbol{r}, t) = \frac{N_1(\boldsymbol{r}, t) \cdot h\nu}{\tau} = \frac{N_0 \sigma F_0(\boldsymbol{r}) \delta h\nu}{\sqrt{1 + \omega^2 \tau^2}} e^{i(\omega\tau - \vartheta)} \tag{5}$$

where $h\nu = E_1 - E_0$ is the energy of the absorbed photon. The product $N_0\sigma$ represents the absorption coefficient of the optical transition, and it is proportional to the gas target concentration. This model requires two assumptions: (i) $F_0(\boldsymbol{r})\sigma$ should be low in order to avoid absorption saturation and neglect stimulated emission; (ii) low-frequency modulation, $\omega \ll 1/\tau$. The first condition is verified for low concentrations of absorbing gas

This article was published in the *Encyclopedia of Analytical Chemistry* in 2021 by John Wiley & Sons, Ltd.
DOI: 10.1002/9780470027318.a9760

and the second one by keeping the modulation frequency in the kilohertz range. The theoretical modeling of the generation of acoustic waves starting from the heat source is well described by Berne and Pecora(13) and requires several approximations to analytically solve the involved differential equations. The natural tendency of the excited system to reach the equilibrium generates two principal types of hydrodynamic modes in the fluid, diffusive and propagating modes. Diffusive modes equilibrate energy through diffusive flux, while propagating modes transfer energy through waves. In terms of thermal or kinetic energy, these modes correspond to thermal diffusion (also referred to as thermal waves) and acoustic relaxation. Let us consider the case of an ideal, uniform, and continuous fluid, perfectly elastic and at the thermodynamic equilibrium except for the local variations of its thermodynamics parameters, small enough to neglect nonlinear effects. The effect of gravitational force is also neglected, so that pressure and density at equilibrium can be considered constant throughout the fluid. The temperature, density, pressure, and linear velocity are defined in terms of small perturbations from equilibrium values:

$$\begin{aligned} T(\boldsymbol{r},t) &= T + \delta T(\boldsymbol{r},t) \\ \rho(\boldsymbol{r},t) &= \rho + \delta\rho(\boldsymbol{r},t) \\ P(\boldsymbol{r},t) &= P + \delta P(\boldsymbol{r},t) \end{aligned} \tag{6}$$

The equilibrium values of temperature (T), density (ρ), and pressure (P) are finite, whereas that of the flow velocity is zero, since the fluid is considered to be at rest except for the induced perturbations. These assumptions simplify the density and energy conservation equations since they contain the terms proportional to the velocity field $\boldsymbol{u}$. The fundamental laws that control the photothermal process are continuity equation (Equation (7a)), the law of momentum (Equation (7b)), and energy (Equation (7c)) conservation, together with the ideal gas law (Equation (7d)):

$$-\frac{1}{\rho}\frac{\partial p}{\partial t} = \boldsymbol{\nabla}\cdot\boldsymbol{v} \tag{7a}$$

$$\rho\frac{\partial \boldsymbol{u}}{\partial t} = -\nabla P + \left(\frac{1}{3}\eta_s + \eta_b\right)\nabla(\boldsymbol{\nabla}\cdot\boldsymbol{u}) + \eta_s\nabla^2\boldsymbol{u} \tag{7b}$$

$$\rho\frac{C_V}{M}\frac{\partial T}{\partial t} + P\,\boldsymbol{\nabla}\cdot\boldsymbol{u} = H \tag{7c}$$

$$\frac{p}{\rho} = (\gamma-1)\frac{C_V}{M}T \tag{7d}$$

where η_s and η_b are the shear and bulk viscosities, respectively, C_V and C_P are the specific heat at constant volume and pressure, respectively, M is the molar mass of the gas molecules, and $\gamma = C_V/C_P$ is the heat capacity ratio. These equations must be solved simultaneously in order to describe changes in pressure, density, and temperature due to gas sample irradiation. A general solution is obtained by reformulating these equations in the form of the Navier–Stokes equations by considering small perturbations of the thermodynamic parameters, fulfilled in photoacoustic effect. By combining Equation (6) and Equations (7a)–(7d), the Navier–Stokes equations can be derived in the form a D'Alembert wave equation describing the propagation of the acoustic mode:

$$\nabla^2\delta p(\vec{r},t) - \frac{1}{c^2}\frac{\partial^2\delta p(\vec{r},t)}{\partial t^2} = -\frac{\gamma-1}{c^2}\frac{\partial H}{\partial t} \tag{8}$$

where c is the sound velocity in the gas. Equation (8) can be solved using the Fourier transform. In this case, it is important to assume that the propagation of the acoustic wave has to be limited to the volume of the photoacoustic cell, which imposes boundary conditions. The Fourier transform of both sides of Equation (8) gives

$$\left(\nabla^2 + \frac{\omega^2}{c^2}\right)\delta p(\boldsymbol{r},\omega) = \frac{\gamma-1}{c^2}i\omega H(\boldsymbol{r},\omega) \tag{9}$$

The general solution can be expressed as a sum of infinite acoustic modes:

$$\delta p(\boldsymbol{r},\omega) = \sum_j A_j(\omega)\delta P_j(\boldsymbol{r}) \tag{10}$$

where $A_j(\omega)$ is the amplitude of the j-mode and $\delta P_j(r)$ solutions of the associated homogeneous wave equation of Equation (9). δP_j must fulfill the boundary condition requiring that $\delta P_j = 0$ at the cell walls, where the pressure waves will exhibit a nodal point. In PAS, the gas is enclosed within an acoustic cell where optical absorption takes place. The calculation of the normal acoustic modes is dependent on the geometry of the acoustic cell, which in turn determines the boundary conditions. Most common acoustic cell designs adopt the basic symmetry of the exciting light source and have a cylindrical shape. The excitation source is a smaller diameter light beam centered along the cylindrical axis. Local pressure propagates radially outward, perpendicular to the exciting beam. When a standing-wave vibrational pattern is created, the acoustic cell acts as an acoustic resonator, which amplifies the acoustic power at the resonance frequency. The degree of amplification of an acoustic cell is described by a quantity called the Q-factor (Q). The Q-factor is expressed as the reciprocal of losses; thus it is a measure of the amount of energy retained in the resonator with respect to the energy dissipated in one cycle. Another common way to express the

Encyclopedia of Analytical Chemistry, Online © 2006–2021 John Wiley & Sons, Ltd.
This article is © 2021 John Wiley & Sons, Ltd.
This article was published in the *Encyclopedia of Analytical Chemistry* in 2021 by John Wiley & Sons, Ltd.
DOI: 10.1002/9780470027318.a9760

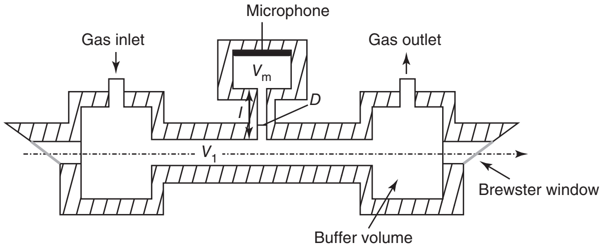

Figure 2 Helmholtz-type geometry cell. Brewster windows and buffer volumes are used to reduce the background noise.

Q-factor is the ratio between the resonance frequency (ω_j) and the full-width half-maximum (FWHM) ($\Delta\omega_j$) of the resonance profile:

$$Q_j = \frac{\omega_j}{\Delta\omega_j} \tag{11}$$

The higher the Q-factor, the better the resonator is. The amplitude of the jth mode corresponding to the resonance frequency ω_j is proportional to

$$A_j(\omega_j) \propto \frac{\gamma - 1}{\omega_j V_0} \alpha P_0 L Q_j \tag{12}$$

where α is the absorption coefficient, P_0 is the optical power of the excitation source, L is the interaction length, and V_0 is the cell volume. Geometries other than cylindrical symmetry have also been employed. Cells that exploit Helmholtz resonances are realized with two chambers, a sample chamber of volume V_1 and a microphone chamber of volume V_m, connected by a cylindrical tube of length I and inside diameter D, as shown in Figure 2.

Typical Q-factors reached by these cells are of the order of ~100 with resonance frequencies of few kilohertz. A microphone is usually placed in the antinode point of one of the eigenmodes of the acoustic cell. The microphone converts the sound wave into an electrical signal, proportional to the amplitude of the detected sound wave. Thus, the electrical signal S can be expressed as

$$S = R_\mathrm{m} \delta P(\boldsymbol{r}_\mathbf{m}, \omega) \tag{13}$$

where R_m is the microphone responsivity and $\delta P(\boldsymbol{r}_\mathbf{m},\omega)$ is the amplitude of the pressure wave in the microphone position. Assuming that the microphone does not alter the acoustic mode of the cavity, Equation (12) can be substituted in Equation (13):

$$S = R_\mathrm{m} \frac{\gamma - 1}{\omega_j V_0} \alpha P_0 L Q_j \delta P(\boldsymbol{r}_\mathbf{m}, \omega) = C_\mathrm{m} \alpha P_0 \tag{14}$$

where C_m is called the cell constant and represents the sensitivity of the whole PAS system. The cell constant depends on the properties of the mechanical resonator (volume, Q-factor, interaction length), the frequency (thus depends on the eigenmodes of the resonator), and the responsivity and position of the microphone. Being the absorption coefficient:

$$\alpha = \sigma N_\mathrm{TOT} c \tag{15}$$

where σ is the molecular absorption coefficient (cm^{-1}), c is the gas target concentration, and N_TOT the molecular density of the mixture, the PAS signal can be expressed as

$$S = C_\mathrm{m} \sigma N_\mathrm{TOT} c P_0 \tag{16}$$

Thus, the electric signal linearly varies with the gas concentration c, allowing quantitative analysis of chemical species. In general, a calibration of the sensor is always performed in order to retrieve the linear coefficient.

4 QUARTZ-ENHANCED PHOTOACOUSTIC SPECTROSCOPY

QEPAS is an alternative method to detect acoustic waves, by means of a QTF instead of a microphone. The use of a QTF has several advantages since the QTF is itself an acoustic resonator, avoiding the use of acoustic resonator cells, thereby removing restrictions imposed on the gas cell design by the acoustic resonance conditions. Moreover, the QTF geometry can be customized to increase the Q-factor and vary the modulation frequency. As shown by Equation (12), the straightforward approach to increase the photoacoustic signal is to reduce the resonance frequency while keeping its Q-factor high. A typical QEPAS apparatus is shown in Figure 3.(14,15)

The laser is focused between the QTF prongs by a plano-convex lens, and the optical power of the laser is monitored through a power meter, for alignment purposes. The acoustic cell is used to confine the analyte gas, which can be toxic or explosive. A gas inlet and outlet are installed to allow gas recycling. The wavelength modulation technique is implemented by applying a sinusoidal dither to the laser current at half of the QTF resonance frequency(16); a transimpedance amplifier is used to acquire the signal from the QTF that is demodulated at the QTF resonance frequency by means of a lock-in amplifier. The lock-in amplifier is usually controlled via a PC by a data acquisition card. The most important advantages of QEPAS include the following features(17,18): (i) a high resonance frequency of the QTF (few tens of kilohertz) combined with a narrow bandwidth (a few Hz at atmospheric pressure) that yields a very high $Q > 10\,000$; (ii) applicability over a wide range of pressure, including atmospheric pressure; (iii) the

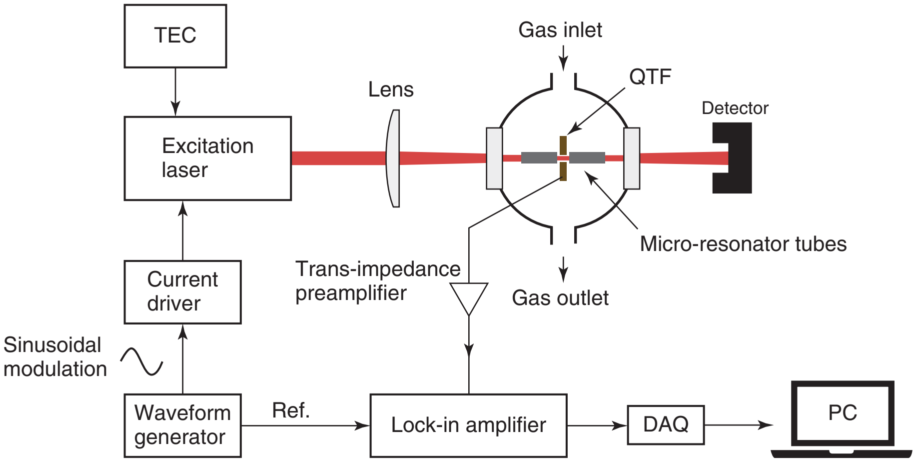

Figure 3 Typical QEPAS set-up. The excitation beam, modulated with a sinusoidal dithering, is focused between the QTF prongs through the microresonator tubes. The electric signal is sent to a lock-in amplifier, which takes the reference from the waveform generator. The demodulated signal is then recorded in a personal computer (PC). DAQ, data acquisition card. (Patimisco et al. 2014(14) and Patimisco et al. 2018(15).)

capability to analyze trace gas samples as low as few cm^3 in volume; and (iv) QTFs are not spectrally sensitive and practically unaffected by environmental noise. Insensitivity to environmental noise in QEPAS derives from two physical phenomena. First, a QTF is an acoustic quadrupole resonator(19) with a bandwidth of few Hertz at normal pressure, thus only an insignificant number of frequency components in this narrow spectral band can produce efficient excitation of the QTF vibrations. Sound waves in air at 32 kHz have an acoustic wavelength of ~1 cm, and, thus, if produced by external acoustic sources, such waves tend to apply a force in the same direction on the two QTF prongs positioned at a distance less than 2 mm. The resulting in-plane symmetric vibrational mode of QTF prongs is not piezoelectrically active and in contrast to the antisymmetric vibration does not yield a detectable signal. Second, ambient noise is generally low above 10 kHz and, therefore, has a minimal effect on the QEPAS signal. In other words, weak environmental noise falls within the analyzed bandwidth. In conclusion, the only way to cause QTF to vibrate via the photoacoustic effect is to produce sound waves from an acoustic source located between the two QTF prongs, as usually done in QEPAS.

4.1 Quartz Tuning Forks

QTFs used in QEPAS set-up exploit the piezoelectric properties of quartz crystal. Piezoelectricity is a phenomenon discovered by Pierre and Jacques Curie, in which noncentrosymmetric crystals can produce an electrical charge upon application of mechanical stress. The opposite is also verified: if an electric voltage is applied to the crystal, mechanical stress is produced. This property arises from the interaction of the external field with the electric dipole moment of the crystal. However, if the material is not a single crystal, individual polarizations cancel each other, and the net polarization is zero. Thus, polycrystalline piezoelectric materials undergo a process named ‘poling’, where the single domains are oriented parallel to each other through an intense external electric field. Standard QTFs have prongs with a length of 3 mm, width of 0.3 mm, and a prong spacing of 300 μm: the fundamental resonance frequency falls at $f \sim 32.7$ kHz. Higher order resonances of standard QTFs cannot be implemented in QEPAS sensors since they would occur at frequencies higher than 190 kHz, and thus not fulfilling the condition $f \ll 1/2\pi\tau$, being τ the time constant of the vibrational-to-translational relaxation of the targeted gas specie in the gas carrier (typically N_2). Time constants are in the microsecond range for many gases.(20) Some gases with slow relaxation rates (CO, CO_2, and NO) do not even fulfill the condition at a frequency as high as 32 kHz.(21) To circumvent this problem, relaxation promoter (such as H_2O or SF_6), i.e. gases that enhance the relaxation rate, can be added to the carrier gas. With this approach, enhancements of nearly two orders of magnitude in QEPAS signal have been reported.(14,22) However, this approach requires additional sensor calibrations and accurate measurements of the promoter concentration. A much more efficient way to solve this limitation consists of realization of custom QTFs with fundamental resonance frequencies <20 kHz, by properly designing the prong geometry. The reduction of the resonance frequency also involves a reduction in the Q-factor; hence a trade-off optimization must be found.(23) The

This article was published in the *Encyclopedia of Analytical Chemistry* in 2021 by John Wiley & Sons, Ltd.
DOI: 10.1002/9780470027318.a9760

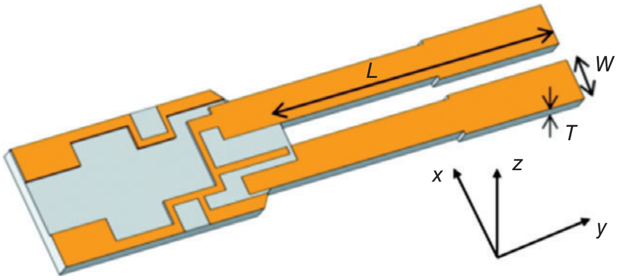

Figure 4 Schematic of a QTF with the reference frame.

resonance frequencies of in-plane flexural modes of the QTF can be calculated by considering an approximation in which each prong of the fork is considered to behave as a cantilever vibrating in the QTF plane (*xy* plane in Figure 4).

Assuming that the Young modulus E, inertia I, and cross-sectional area A are constant along the cantilever, the natural vibrations are ruled by the Euler–Bernoulli equation:

$$EI\frac{\partial^4 y(z,t)}{\partial z^4} + \rho A\frac{\partial^2 y(z,t)}{\partial t^2} = 0 \tag{17}$$

where $E = 72\,\text{GPa}$ is the component of the quartz Young's modulus in the vibration plane of the QTF, $\rho = 2649\,\text{kg}\,\text{m}^{-3}$ is the density of quartz, t is the time, and $A = w \times L$, w and L are the prong thickness and length, respectively, while xy plane contains the QTF. With two boundary conditions, Equation (17) can be greatly simplified. Both boundary conditions come from the support of the QTF. The fixed end must have zero displacement and zero slope due to the clamp, while the free end cannot have a bending moment or a shearing force. The resonance frequencies in vacuum f_n are thus obtained as a solution of Equation (17)(24):

$$f_n = \frac{\pi T}{8\sqrt{12}L^2}\sqrt{\frac{E}{\rho}}\nu_n^2 \tag{18}$$

where $\nu_0 = 1.194$ for the fundamental mode (lowest flexural oscillation mode) and $\nu_1 = 2.988$ for the first overtone mode. The lateral displacements of vibrating prongs at the fundamental and overtone modes are shown in Figure 5(a) and (b), respectively.(25)

The Q-factor of a resonance mode is a measure of energy loss occurring while prongs are vibrating. Three main loss mechanisms contribute to the overall Q-factor: (i) air damping, $1/Q_{\text{air}}$, related to the transfer of energy and momentum from the QTF prongs to the surrounding medium(26); (ii) support loss, $1/Q_{\text{sup}}$, related to the transfer of mechanical energy from the vibrating prong to the support(27); (iii) thermoelastic damping, $1/Q_{\text{TED}}$, related to coupling between strain and temperature field inside the QTF.(28) Since the dissipation mechanisms are assumed independent of each other and the resonator Q-factor is proportional to the inverse of the total energy dissipated, the overall Q-factor can be represented as(29,30) follows:

$$\frac{1}{Q} = \frac{1}{Q_{\text{air}}} + \frac{1}{Q_{\text{sup}}} + \frac{1}{Q_{\text{TED}}} \tag{19}$$

These contributions have been individually studied, and it can be proved that they mostly depend on the QTF geometry and the gas pressure. The latter has a significant influence on the Q-factor since air damping can effectively reduce the Q-factor and influence the resonance frequency. Indeed, the QTF mainly loses energy via the interaction with the surround viscous medium. A good approximation for the dependence of the Q-factor on the gas pressure is provided by the following equation(29,30):

$$Q(P) = \frac{Q_0}{1 + Q_0 b\sqrt{P}} \tag{20}$$

where Q_0 is the Q-factor at $P = 0$, which includes all pressure-independent loss mechanisms (support losses and thermoelastic damping), and b is a fitting parameter. Both Q_0 and b are mainly related to QTF geometry and gas viscosity, thus vary for each QTF. As an example, typical Q-factors in vacuum are on the order of 10^5, while at ambient pressure it is reduced to approximately 10^4. The dependence of the resonance frequency to the surround gas pressure can be determined by the assumption that the gas effect on prong vibrations damping increases the inertia of the mass prong. Thus, the Euler–Bernoulli equation in Equation (17) requires an additional term corresponding to the reactive part, which attributes additional inertia to the vibrating prong(24):

$$EI\frac{\partial^4 y(z,t)}{\partial z^4} + (\rho A + u)\frac{\partial^2 y(z,t)}{\partial t^2} = 0 \tag{21}$$

where u is the added mass. The eigenfrequency f_n of the fundamental mode changes as

$$f_n = f_{n,v}\left(1 - \frac{1}{2}\frac{u}{\rho A}\right) \tag{22}$$

where $f_{n,v}$ is determined in vacuum by Equation (18). The exact derivation of the added mass u is a complicated problem even for simple prong structures. The added mass per unit length of a thin prong has been found proportional to gas density ρ_0.(31) By using the ideal gas law, the gas density can be expressed by $\rho_0 = MP/RT_{\text{a}}$, where M is molar mass, P is the gas pressure (in Torr

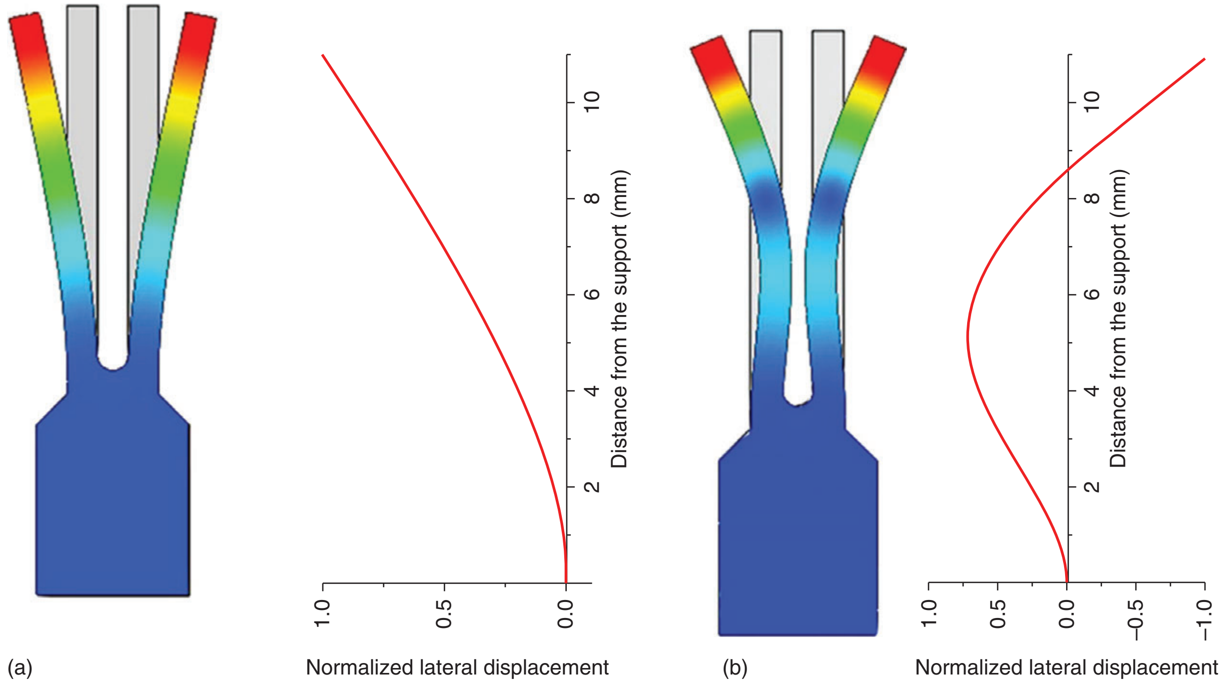

Figure 5 Representation of the flexural (a) fundamental mode and (b) first overtone mode. The normalized lateral displacement along the tuning fork prong is shown. (Based on Tittel et al. 2016(25).)

unit), $R = 62.3637\,\mathrm{m^3\ Torr\,K^{-1}\,mol}$ is the gas constant, and T_a is the prong temperature (in K). Thus, the QTF resonance frequency shifts linearly with the pressure, if the temperature is supposed fixed.

The electric properties of the QTF can be derived with an electric model equivalent to the mechanical model. Due to piezoelectricity, strain field and electric field in the material are linked together. Thus, the QTF is both a circuit with capacitance C_Q, resistance R_Q, and inductance L_Q and equivalently a mass m on a spring with spring constant k and damping factor β. The QTF electric model is an RLC series circuit with the resonance frequency and Q-factor given by

$$f_0 = \frac{1}{2\pi}\sqrt{\frac{1}{L_Q C_Q}}$$

$$Q = \frac{1}{R_Q}\sqrt{\frac{1}{L_Q C_Q}} \qquad (23)$$

The electric charges accumulate on both faces of the tuning fork prongs in a quadrupole configuration and are extracted by chromium/gold layers that act as electrodes.

Recently, new prong geometries have been proposed to enhance the resonance properties of QTF at lower frequencies. Moving to low resonance frequencies by varying the ratio T/L (Figure 4) following the Euler–Bernoulli equation for rectangular prongs, the Q-factor decreases.(23) In particular, QTFs with a resonance frequency lower than 10 kHz cannot ensure $Q > 10\,000$ at atmospheric pressure. A further reduction in resonance frequency with slight modifications of the overall Q-factor requires a change in the prong geometry. T-shaped prongs have been proposed to accomplish both requirements, with a further increase in the stress field distribution along vibrating prongs with respect to rectangular prongs, beneficial for piezoelectric charge generation when prongs are deflected.(32–34) In addition, applying rectangular grooves in prongs increases the electrical coupling between electrodes, leading to a reduction in the electrical resistance without affecting the Q-factor.(35)

4.2 Acoustic Resonator Tubes

The QTF is not used as a standalone in a QEPAS sensor, but typically it is acoustically coupled with a pair of millimeter-sized resonator tubes (mRs) located on both sides of the QTF, as sketched in Figure 6.

This arrangement is known as the on-beam QEPAS configuration. Conversely, in the off-beam configuration, a single resonator tube is positioned adjacent to the QTF: the QTF senses the pressure in the microresonator through a small aperture in its center.(36,37) Resonator tubes act as an acoustic resonator: the standing-wave

Encyclopedia of Analytical Chemistry, Online © 2006–2021 John Wiley & Sons, Ltd.
This article is © 2021 John Wiley & Sons, Ltd.
This article was published in the *Encyclopedia of Analytical Chemistry* in 2021 by John Wiley & Sons, Ltd.
DOI: 10.1002/9780470027318.a9760

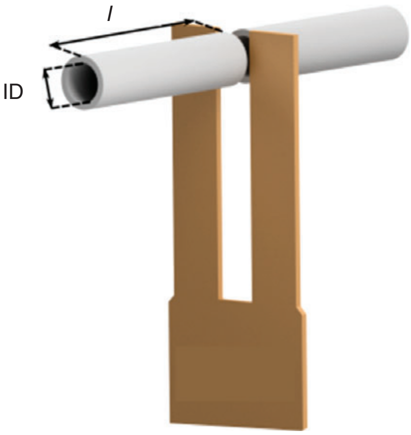

Figure 6 Schematic diagram of the QEPAS spectrometer.

vibrational pattern within the tubes enhances the intensity of the acoustic field between the QTF prongs up to 60 times.(23) The QTF coupled with a single or a pair of resonator tubes constitutes the QEPAS spectrophone and represents the core of any QEPAS detection module. In the on-beam configuration, when two tubes are acoustically coupled with a QTF, the internal diameter (ID) of the tubes and their length influence the enhancement of the sound wave between the QTF prongs. Dello Russo et al.(38) proposed a theoretical model to predict the optimal tube diameter, in which the acoustic coupling between two tubes is expressed in terms of the amount of the acoustic field transferred from one tube to the other one. As a result, the optimal tube radius strongly depends on the sound wavelength λ_s and the prong spacing g. As an example, for a QTF resonating at 8 kHz in pure SF_6 ($\lambda_s = v_s/f_0 = 16.7$ mm, being $v_s = 136\,\mathrm{m\,s^{-1}}$ the speed of sound in the SF_6 gas and $g = 800\,\mu\mathrm{m}$), the theoretical model predicts an optimal ID = 1.0 mm. The optimal tube length can be estimated by considering the open-end correction, which assumes that the antinode of a standing sound wave in an open-ended resonator is located outside the tube end, due to an impedance mismatch between the acoustic field inside the resonator and outside. The optimal tube length l depends on the tube ID and the sound wavelength by the relation(39)

$$l = \frac{v_s}{2f_0} - \frac{8\,\mathrm{ID}}{3\pi} \tag{24}$$

Thereby, the optimal tube length depends on the tube ID, the speed of sound v_s, and the resonance frequency f_0 of the acoustic wave.

4.3 Overtone Modes

In QEPAS sensing, the resonance frequency of the QTF must be limited to below 40 kHz to ensure that the transfer of the excess energy absorbed by the target gas follows efficiently the fast modulation of the incident laser radiation. The first overtone mode frequencies can be reduced by playing on the prongs' geometry, with a decrease in the fundamental resonance frequency down to few kilohertz. This led to the implementation of QTF overtone flexural modes for QEPAS trace gas sensing. By using Equation (18), the first overtone mode frequency is ~6.2 times higher than the fundamental mode. The first demonstration of QEPAS system exploiting a QTF operating in the first overtone flexural mode is reported by Sampaolo et al.(40) In this case, a QTF having a fundamental resonance frequency at 2.8 kHz and a first overtone mode at 17 kHz was implemented in a QEPAS-based sensor system operating in the near-IR spectral range. The selected target gas was water vapor and allowed a comparison of the QEPAS signal using both the fundamental and first overtone QTF flexural modes. The two modes exhibit different Q-factors because the loss mechanisms depend on both the resonance frequency and the vibrational dynamics of the resonance mode. As discussed, the dominant loss mechanism is vibration damping due to the medium surrounding the vibrating QTF. The damping dynamics are derived from the Navier–Stokes equation and the continuity equation for incompressible fluids. When the prongs are oscillating at the nth natural flexural frequency f_n, the Q-factor associated with air damping Q_{air} can be assumed to be proportional to(26)

$$Q_{\mathrm{air}} \propto \frac{4\pi\rho T w^2 f_n}{3\pi\mu w + \frac{3}{4}w^2\sqrt{4\pi\rho_a \mu f_n}} \tag{25}$$

where ρ_a is the air density and μ is the air viscosity. Q_{air} increases with the resonance frequency since the air damping effect decreases with an increasing overtone mode order n. Thereby, for a QTF, air damping mechanisms are strongly reduced when prongs vibrate in the overtone mode with respect to the fundamental mode. The second loss mechanism considered for a vibrating QTF is support losses. Support losses are due to dissipation of the prong vibrational energy through its support. Hence, support losses are influenced by the vibrational dynamics of the resonance mode. In terms of the Q-factor, the contributions of extrinsic and intrinsic loss mechanisms depend on the vibrational dynamics of the selected resonance mode since each vibrational mode can be characterized by different distributions of its effective mass. The fundamental in-plane flexural mode can be represented by a single point-mass on the prong tip, while the first overtone can be considered a system of two

Encyclopedia of Analytical Chemistry, Online © 2006–2021 John Wiley & Sons, Ltd.
This article is © 2021 John Wiley & Sons, Ltd.
This article was published in the *Encyclopedia of Analytical Chemistry* in 2021 by John Wiley & Sons, Ltd.
DOI: 10.1002/9780470027318.a9760

coupled point-mass subsystems located at two antinodes. The different distribution of the effective mass mainly affects the support losses. Since the dimensions of the support are assumed to be much larger than those of the prong, flexural vibrations can be treated using the single cantilever beam theory. The contribution of the Q-factor due to support losses is given by(26)

$$Q_{\text{sup}} \propto \frac{1}{k_n^2}\left(\frac{L}{T}\right)^3 \tag{26}$$

where k_n is a constant that increases as the mode number increases. Hence, Q_{sup} is mainly influenced by the ratio between the prong length and its thickness and decreases for higher order modes. For overtone modes, the higher the L/T ratio, the lower will be the mechanical stress onto the QTF support. To reduce the support losses of the overtone modes, the factor $(L/T)^3$ should be increased, leading to an increase in the air damping losses, affecting negatively the overall Q-factor. Thus, even if the support losses increase with the mode number, it is possible to obtain a larger Q-factor for overtone modes with respect to the fundamental mode by optimizing the dimensions of the QTF prongs to strongly reduce the air damping mechanisms, which are the dominant loss mechanism.(30) Different from a fundamental flexural mode, the first overtone mode oscillation shows two antinodes (Figure 5b), oscillating in the counter phase. Hence, it is possible to excite two resonance antinode points simultaneously by using two laser beams if their phase shift is properly adjusted. The first demonstration of a double-antinode excited quartz-enhanced photoacoustic spectroscopy (DAE-QEPAS) system was reported by Zheng et al.,(41) implementing a custom QTF having the fundamental and first overtone flexural modes resonance frequencies at 2.8 and 17.7 kHz, respectively. The QTF is positioned between the two mR tubes to probe the acoustic vibration excited in the gas inside the tubes and the two mRs are positioned at the heights corresponding to the lower and higher QTF first overtone resonance antinode points, as schematically shown in Figure 7.

A pigtailed distributed feedback (DFB) laser emitting at 1.37 μm was used to generate the photoacoustic signal, by exciting a H_2O absorption line located at 7306.75 cm^{-1} with a line intensity of 1.8×10^{20} cm mol^{-1}. A piezotransducer phase compensator was used to adjust the phase between the two laser beams passing through the two mR tubes in order to maximize the QEPAS signal. The phase shift between the two antinode points is ~180°. The laser beam passed twice through the lower mR and once through the upper mR, exciting the two QTF resonance antinodes simultaneously with a compensated phase. The largest QEPAS signal-to-noise ratio (SNR) was obtained using 8.5-mm-long tubes for the two mRs. The achieved signal amplitude was ~3 times higher than that obtained with standard on-beam QEPAS, ~100 times that obtained with a bare QTF operating at the first overtone mode, and ~500 times higher when operating at the fundamental flexural mode resonance.

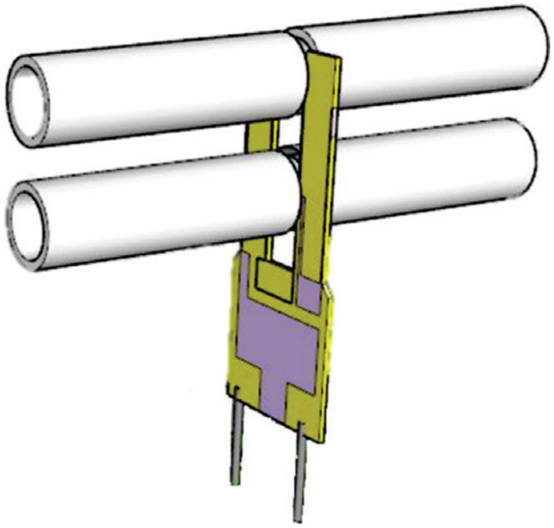

Figure 7 Schematic of the spectrophone implementing a couple of microresonator tubes aligned perpendicularly to the QTF. The first pair of tubes is located at the overtone mode antinode point near the QTF top, the second pair is positioned slightly below the center of the prongs, at the second antinode point position of the QTF first overtone mode.

The simultaneous excitation of the QTF both on the fundamental and first overtone modes, using the same or two different laser sources paved the way to simultaneous dual-gas detection. This approach was employed in the first demonstration of simultaneous dual-gas sensing, based on a QTF frequency-division multiplexing (FDM) technique.(42) The QTF in a dual-gas QEPAS sensor is excited simultaneously at the fundamental and first overtone flexural modes by two independently modulated lasers. The two target gases are detected via demodulation of the custom QTF piezoelectric signal at the fundamental frequency f_0 and the first overtone frequency f_1, respectively, by two lock-in amplifiers. The focused beams were positioned near the antinode point for the fundamental flexural mode and close to the first overtone flexural mode lower antinode point (Figure 5b), respectively. The QTF was connected to a custom transimpedance amplifier, which delivered the amplified signal to two lock-in amplifiers for wavelength modulation detection. A preliminary test with both laser sources tuned to the same wavelength at 1.368 μm, resonant with a water absorption line was performed to verify that there were no cross-talking effects between the fundamental

This article was published in the *Encyclopedia of Analytical Chemistry* in 2021 by John Wiley & Sons, Ltd.
DOI: 10.1002/9780470027318.a9760

and the first overtone flexural mode QEPAS signals, when the QTF was operated in the combined vibrations. No interference effects and no excess noise were observed when the QTF operated in combined vibrational motion with respect to the pure fundamental or first overtone flexural mode. The capability of the QEPAS sensor to perform simultaneous dual-gas spectral detection was demonstrated by implementing a DFB laser source targeting an acetylene (C_2H_2) absorption line located at 6541.96 cm^{-1} and the diode laser targeting a H_2O absorption line. The QEPAS spectra of both H_2O and C_2H_2 were acquired continuously without signal cross-talking. Recently, a dual-gas QEPAS sensor capable of simultaneous detection of water vapor and alternatively methane or nitrous oxide has been reported.(43) A diode laser and a quantum cascade laser (QCL) excited independently and simultaneously both the fundamental and the first overtone flexural modes of the QTF, respectively. The diode laser targeted a water absorption line located at 7181.16 cm^{-1} (1.392 μm), while the QCL emission wavelength was centered at 7.71 μm and was tuned to target two strong absorption lines of methane and nitrous oxide, located at 1297.47 and 1297.05 cm^{-1}, respectively. Two sets of microresonator tubes were positioned, respectively, at the antinode points of the fundamental and the first overtone flexural modes of the QTF to enhance the QEPAS signal-to-noise ratio. Detection limits of 18 ppb for methane, 5 ppb for nitrous oxide, and 20 ppm for water vapor have been achieved with a lock-in integration time of 100 ms.

5 QUARTZ-ENHANCED PHOTOACOUSTIC SPECTROSCOPY SENSORS FOR REAL-WORLD APPLICATIONS

High selectivity and detection sensitivity and short response time are the primary requirements for trace gas sensing. These characteristics together with no need for recalibration, the absence of any degradable component, portability, and low cost are strict requirements for a gas sensor system to be particularly suitable for on-field applications such as environmental monitoring, breath sensing, leak detection, industrial processes control, and oil and gas exploration.(44)

Several QEPAS sensors have been realized for environmental monitoring and many of them tested out-of-laboratory. A QEPAS sensor was used to perform real-time and in situ atmospheric measurements of CH_4 and N_2O.(45) The QEPAS-based sensor system used a 7.83-μm CW, thermoelectrically cooled (TEC) QCL, with an output power of 158 mW. The QEPAS spectrophone was composed of a commercial 32.7-kHz QTF acoustically coupled with a dual-tube mR system. MDLs of 13 ppb for CH_4 and 6 ppb for N_2O were reached. After the evaluation of its performance in laboratory environment, the developed QEPAS sensor was then installed in the Aerodyne Research, Inc. mobile laboratory (AML) to perform CH_4 and N_2O atmospheric concentration measurements near an urban solid waste disposal site in Greater Houston, Texas (WM Atascocita and BFI McCarty landfills). The average CH_4 mixing ratio detected near the BFI McCarty landfill was ∼5 ppm based on averaging over measurements during the morning time, while the highest mixing ratios observed, 16 and 27 ppm, were related to waste trucks passing near the AML. Another QEPAS sensor for simultaneous detection of CH_4 and H_2O vapor by an FDM technique, in which a custom QTF was operated in the fundamental and first overtone combined vibration modes, was reported by Wu et al.(46) Continuous field measurements were carried out near the largest sanitary landfill in Shanxi province, China. A simple algorithm was developed to normalize the influence of H_2O molecules on the methane nonradiative energy relaxation rate. Elefante et al.(47) proposed a dual-gas sensor based on the combination of a QEPAS sensor and an electronic hygrometer for the simultaneous detection of CH_4 and water vapor H_2O in air. The QEPAS sensor used an interband cascade laser operating at 3.34 μm capable of targeting a CH_4 absorption line at 2988.8 cm^{-1} and a water line at 2988.6 cm^{-1}. Water vapor was measured with both the electronic hygrometer and the QEPAS sensor for comparison. The sensor was tested by performing prolonged measurements of CH_4 and H_2O over 60 h to demonstrate the effectiveness of this approach for environmental monitoring applications. Another example of QCL-based QEPAS sensor targeting a gas molecule relevant for environmental monitoring is reported by Giglio et al.(48) An array of 32 pulsed DFB QCLs emitting in the 1190–1340 cm^{-1} spectral range was used as the excitation source of a QEPAS sensor in the on-beam configuration for nitrous oxide broadband detection. At a duty cycle of 0.75%, the highest optical power measured among the 32 devices was 1.6 mW. With a 10-s lock-in integration time, a detection limit of less than 60 ppb was achieved, matching the sensitivity level required for nitrous oxide monitoring at global atmospheric levels. The same QEPAS sensor was used to detect methane. The QEPAS spectral scan of 1000 ppm of $N_2O:N_2$ and 1000 ppm of $CH_4:N_2$ are reported in Figure 8(a) and (b), respectively.

The QEPAS scan of the N_2O reconstructs the N_2O P- and R-branch centered at 1270 and 1298 cm^{-1}, with a minimum at 1287 cm^{-1} corresponding to the forbidden *Q*-branch. Conversely, methane exhibits an uneven absorption spectrum composed of several lines differing both in line-strength and in wavenumber spacing. Regarding

This article was published in the *Encyclopedia of Analytical Chemistry* in 2021 by John Wiley & Sons, Ltd.
DOI: 10.1002/9780470027318.a9760

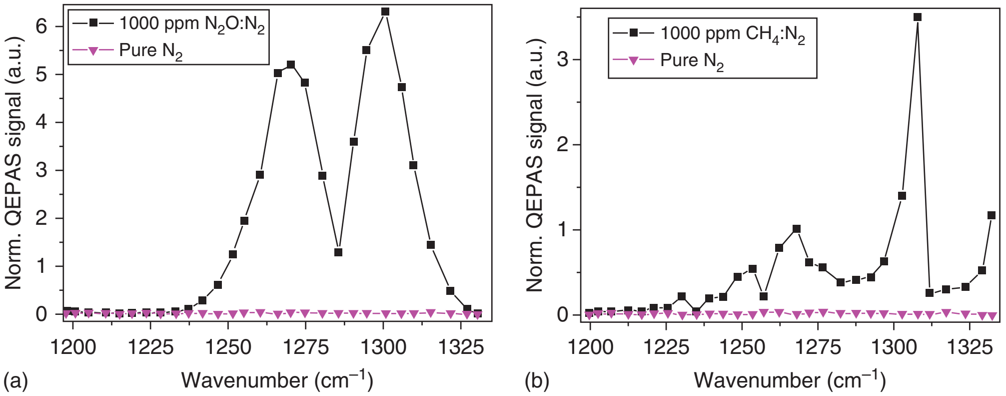

Figure 8 (a) 1000 ppm (black squares) of N_2O QEPAS signal normalized by the laser optical power is plotted as a function of the laser wavenumber. The QEPAS signal measured for pure N_2 (pink triangles) is also reported. (b) 1000 ppm (black squares) of CH_4 QEPAS signal normalized by the laser optical power is plotted as a function of the wavenumber together with QEPAS signal measured for pure N_2 (pink triangles).

broadband detection, Zhou et al. demonstrated QEPAS detection of chlorodifluoromethane ($CHClF_2$) and acetone (C_3H_6O) in the 1180–1345 cm^{-1} spectral region by exploiting the tunability range of an external cavity QCL.(49) In this example, each target molecule exhibits unresolved rotational–vibrational absorption lines. However, the absorption features of the two molecules lie in apart spectral regions.

For the petrochemical industry, monitoring of hydrocarbons such as methane, ethane, and propane represents one of the most efficient ways to predict production outputs, estimate reserves, assess raw material quality of source rocks and reservoirs. For the analysis of downhole hydrocarbon mixture compositions, spectroscopic measurements are usually not performed on single-gas component samples but on multicomponent mixtures. The commercial availability of interband cascade lasers has led to new opportunities for trace detection of the main hydrocarbon gases. Indeed, the fundamental absorption bands of methane, ethane, propane, ethylene, propene, and acetylene are located in the $\lambda = 3$–$4\,\mu m$ spectral range. A QEPAS sensor system designed to detect methane, ethane, and propane using a single interband cascade laser emitting in the spectral range 3.342–3.349 μm was reported by Sampaolo et al.(50) The QEPAS sensor achieved an ultimate detection limit of 90 ppb, 7 ppb, and 3 ppm for CH_4, C_2H_6, and C_3H_8, respectively, for a 1-s integration time. Ethane detection was also reported by Sgobba et al.(33) by using a QEPAS sensor and a custom pigtailed laser diode emitting at ~1684 nm as the exciting light source. The QEPAS spectrophone consisted of a custom 12.4-kHz QTF coupled with a pair of mR tubes each having a length of 12.4 mm and an ID of 1.6 mm. The MDL reached with a 100-ms lock-in integration time was 22 ppm. The dynamic range of a CW DFB QCL has been exploited to selectively detect isotopes $^{12}CH_4$ and $^{13}CH_4$ in methane samples at the natural abundance in the 1296.00–1296.15 cm^{-1} spectral range.(51) Isotopic ratio can be used as a fingerprint and an indicator for many processes involving isotopic fractionations. The thermogenic or biogenic origin of natural gas, as well as its source and history, can be identified by measuring the methane isotopic ratio. Therefore, with a sensitivity at the parts-per-billion level, this sensor opens the way to the development of QEPAS-based gas spectrometers to be used downhole for oil and gas exploration.

For industrial process control, gas leak detection and its localization play an important role in all the industrial fields requiring manufacturing quality-control processes. Leak detection requires techniques that do not damage the characteristics or performance of components such as vessels, valves, pipes, or rubber seals. In 2016, a gas leak detector based on the QEPAS sensor was developed to test mechatronic systems and components, such as vacuum valves and diesel injectors, usually operating at high pressures.(52) Leak tightness requirements are extremely important in automotive industry to lower emissions and improve fuel consumption. The sensor employed sulfur hexafluoride (SF_6) as leak tracer gas due to its properties of being extremely stable, inert, nonflammable, nontoxic, particularly suitable and safe for working environment.(53) A QCL in the external cavity configuration, resonant with a strong SF_6 absorption band around 947 cm^{-1}, was used as the excitation source. The QEPAS sensor was integrated into a vacuum-sealed test station. A calibrated leak (ATEQ, model L1147AQ-N) was used to validate the test station. The leak flow measured by the QEPAS sensor as a function of the differential pressure is reported in Figure 9(a).

Encyclopedia of Analytical Chemistry, Online © 2006–2021 John Wiley & Sons, Ltd.
This article is © 2021 John Wiley & Sons, Ltd.
This article was published in the *Encyclopedia of Analytical Chemistry* in 2021 by John Wiley & Sons, Ltd.
DOI: 10.1002/9780470027318.a9760

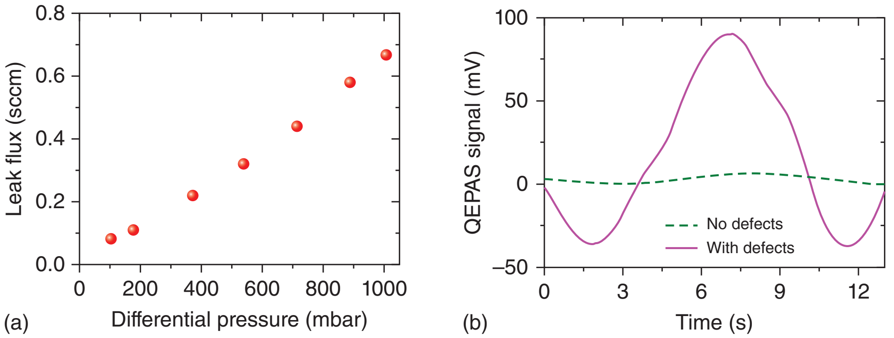

Figure 9 (a) Leak flows measured as a function of differential pressure using the QEPAS sensor. (b) QEPAS scans of the SF_6 absorption line centered at 947.93 cm^{-1} measured when the test station is vacuum sealed (green dotted line) and when a defect, a wire of 20-μm diameter, is inserted in the system (fuchsia solid line).

In the absence of any defect, the test station is vacuum-tight. A local defect was created by inserting a small metallic wire of 20-μm diameter, which compromises the vacuum seal. The QEPAS spectral scan of the SF_6 absorption line obtained for the test station without defects and with defects are reported in Figure 9(b). Validation tests showed a minimum detection sensitivity of 2.75 ppb for a 1-s integration time, corresponding to a minimum detectable leak of 4.5×10^{-7} mbar L s^{-1}, for a nitrogen gas carrier flow of 0.67 mbar L s^{-1}. If pure SF_6 is used as leak test gas, sensitivity can be improved down to ~4.5×10^{-9} mbar L s^{-1}. In terms of sensitivity, QEPAS performance was competitive with most of the gas leak detection techniques reported in the literature.(53) Another example of QEPAS sensor employed in industrial process control was reported by Shi et al.(54) A compact and sensitive mid-infrared nitric oxide (NO) sensor was designed by using a DFB QCL emitting at 1900.07 cm^{-1} with an optical power of 65 mW. With an MDL of 120 ppb, for a lock-in integration time of 1 s, the QEPAS NO sensor was deployed for real-time diesel-engine exhaust monitoring. Measurements were performed by sampling the exhaust of an ISUZU LT 134L bus diesel engine (6HK1-TC Euro-III Compliant Rear Engine) at the Chinese University of Hong Kong. A slight decrease in the QEPAS signal was observed due to scattering of the laser light by soot particles, highlighting the importance of integrating a soot filter at the sensor inlet. An increase in NO concentrations from 126 to 187 ppm in the exhaust was measured when the engine rotational speed increased from 500 to 2000 revolutions per minute.

Clinical and biomedical applications require smart and portable gas sensors. Human breath analysis techniques can offer a potential revolution in health-care diagnostics. In principle, each breath contains information regarding the internal state of a patient. The technical challenge facing both clinicians and measurement system providers is to extract from that breath meaningful data, which can be correlated to patients' health. Benchtop instrumentations such as mass spectrometers can use laboratory settings to provide a baseline correlation between exhaled species and physical conditions. However, to fully realize the potential of breath analysis as a patient diagnostic tool, its application must take place not only in the laboratory but also in the clinic and at home. Human breath is composed of a matrix of nitrogen, oxygen, water vapor, carbon dioxide, and inert gases (Ar, Ne, He) where a mixture of as many as 500 molecules is diluted in traces concentrations. The presence of some molecules or metabolites in the exhaled molecular profile, such as NH_3, C_2H_4, CS_2, or NO in elevated concentrations compared to the normal ones, is closely associated with inflammatory processes and diseases.(55–58) A QEPAS sensor for ethylene detection was reported, employing a CW DFB-QCL, emitting at 967.40 cm^{-1} with an optical power of 74.2 mW, and an optimized spectrophone in the on-beam configuration.(59) The best working pressure for high-sensitivity C_2H_4 detection was found to be 120 Torr. At 10-s lock-in integration time, a sensitivity of 10 ppb was achieved, comparable to the C_2H_4 concentration levels in breath indicative of lipid peroxidation in lung epithelium. Another example reported a CW DFB-QCL emitting at 2178.69 cm^{-1} with an optical power of 75 mW employed as light source for QEPAS sensor to detect carbon disulfide (CS_2), a biomarker of respiratory bacterial colonization in cystic fibrosis.(60) Here, an MDL of 28 ppb was achieved for a lock-in integration time of 1 s when the gas sample was moisturized with a water vapor concentration of 2.3 vol%, to improve the gas vibrational–translational relaxation process, at a pressure of 56 Torr. A QEPAS sensor employing a widely tunable, mode-hop-free, external cavity, QCL was realized for NO detection at 1900.08 cm^{-1} with an optical excitation

This article was published in the *Encyclopedia of Analytical Chemistry* in 2021 by John Wiley & Sons, Ltd.
DOI: 10.1002/9780470027318.a9760

power of 66 mW.(22) A NO detection sensitivity of 4.9 ppb by volume was achieved with a 1-s lock-in integration time, by adding a 2.5% of water vapor concentration, at 250 Torr. These sensors represent a proof-of-concept on the great potential of QCL-based QEPAS as a powerful breath sensing technique. The first clinical study of a QEPAS-based breath sensor was performed at the St. Luke's University Hospital of Bethlehem, PA, USA, in 2013.(61) In this study, breath ammonia was detected with a fast, real-time monitor using a CW DFB QCL-based QEPAS sensor coupled to a breath sampling device that measures mouth pressure and the real-time concentration of carbon dioxide. The selected laser source allows the 967.35 cm^{-1} NH_3 absorption line to be targeted with an optical power of 24 mW. At a working pressure of 120 Torr, a detection sensitivity as low as 6 ppb was achieved with a 1-s lock-in integration time. The NH_3 QEPAS sensor was used to evaluate the potential clinical utility of breath ammonia compared to blood ammonia. In particular, a protocol was used to study the effects that the mode of breathing and the mouth pH have on the determination of exhaled breath ammonia. Recently, the first carbon monoxide QEPAS sensor dedicated to human breath analysis was tested at the Montpellier University Hospital, Montpellier, France.(62) The developed sensor employed a CW Fabry–Perot QCL emitting at 2103.26 cm^{-1} with an optical power of 80 mW. The achieved sensitivity at atmospheric pressure and at a lock-in integration time of 1 s was 20 ppb. The performance of the QEPAS sensor was compared with reference methods. The obtained results confirmed the ability of the QCL-based QEPAS sensor for measuring low-level endogenous exhaled CO concentrations.

Human breath samples face with absorption spectra with unresolved rotational–vibrational absorption features. When molecules exhibit a strong absorption features overlap, instead, multigas sensing can represent a challenge. Linear regression of the QEPAS signal as a function of gas concentration is efficient as long as the experimental data are uncorrelated or at least weakly correlated; otherwise, there can be a lack of precision and accuracy. To address this issue, an algorithm based on partial least squares regression (PLSR) was proposed by Zifarelli et al.(63) to retrieve the components concentration in a three-gas mixtures. Here, a CW DFB QCL was employed as the excitation source of a QEPAS sensor for environmental relevant gases detection. Analyzed gas mixtures were composed of different amounts of acetylene, methane, and nitrous oxide, showing a spectral overlap greater than 97% in the laser emission range (1295.5–1296.5 cm^{-1}). The calibration error reported for the three-gas component concentrations predicted by the PLSR tool is up to five times better compared with standard linear regression.

6 CONCLUSIONS AND FUTURE PERSPECTIVES

This article focused on recent advances in the QEPAS sensing technique for the detection and monitoring of trace gas species. In the first part, the relevant basic principles were revisited. In standard PAS, the sound detector is a noisy microphone and the acoustic resonance is imposed by the geometry of the acoustic cell. QEPAS overcomes these impositions: a millimeter-sized spectrophone acts as both detector and acoustic resonator, resulting in a high-compact and low-cost detection module with high immunity to ambient noise. Moreover, the piezoelectric readout is largely favored than an interferometric readout occurring in cantilever-based PAS as the latter adds more complexity and lower mechanical stability to the set-up. As an absorption spectroscopy technique, a large discussion was dedicated to the advantages of this approach, in terms of selectivity, sensitivity, and possibility for optical sensing without an optical detector. Progress to date in terms of development of custom QTFs as well as new approaches for QEPAS sensing were presented. Compared with a 32-kHz QTF coupled with a micrometer-sized resonator tubes, the development of custom tuning forks resulted in better QEPAS sensing performance and reduced the resonance frequency down to few kilohertz allowing to efficiently remove limitations in terms of detection of slow-relaxer gases such as CO, CH_4, and NO. Furthermore, the possibility to increase the prong spacing makes the optical alignment less critical, especially with laser sources having poor spatial beam quality. The reduction of the fundamental flexural mode resonance in custom QTFs has opened the way to the exploitation of the first overtone mode for QEPAS sensing. This leads to demonstration of new approaches such as simultaneous dual-gas detection, thanks to the possibility to excite the QTF simultaneously at the fundamental and the first overtone flexural modes. Today, many researchers and development teams are still working on improving the performance and devising new methods to exploit different QEPAS configurations.

ABBREVIATIONS AND ACRONYMS

AML	Aerodyne Research, Inc. Mobile Laboratory
$CHClF_2$	Chlorodifluoromethane
CS_2	Carbon Disulfide
CW	Continuous-wave
DAE-QEPAS	Double-antinode Excited Quartz-enhanced Photoacoustic Spectroscopy

This article was published in the *Encyclopedia of Analytical Chemistry* in 2021 by John Wiley & Sons, Ltd.
DOI: 10.1002/9780470027318.a9760

DFB	Distributed Feedback
FDM	Frequency-division Multiplexing
FWHM	Full-width Half-maximum
ID	Internal Diameter
MDL	Minimum Detection Limit
mR	Millimeter-sized Resonator Tube
NEC	Noise Equivalent Concentration
NNEA	Normalized Noise Equivalent Absorption Coefficient
NO	Nitric Oxide
PAS	Photoacoustic Spectroscopy
PLSR	Partial Least Squares Regression
ppb	Parts Per Billion
Q-factor	Quality Factor
QCL	Quantum Cascade Laser
QEPAS	Quartz-enhanced Photoacoustic Spectroscopy
QTF	Quartz Tuning Fork
SNR	Signal-to-noise Ratio
TEC	Thermoelectrically Cooled

RELATED ARTICLES

Environment: Trace Gas Monitoring
Diode Laser Spectroscopic Monitoring of Trace Gases • Environmental Trace Species Monitoring: Introduction • Laser Absorption Spectroscopy, Air Monitoring by Tunable Mid-Infrared Diode • Optical Gas Sensors in Analytical Chemistry: Applications, Trends and General Comments • Photoacoustic Spectroscopy in Trace Gas Monitoring

Environment: Water and Waste
Detection and Quantification of Environmental Pollutants • Infrared Spectroscopy in Environmental Analysis

Field-portable Instrumentation
Field-portable Instrumentation

Industrial Hygiene
Sensors in the Measurement of Toxic Gases in the Air

Infrared Spectroscopy
Theory of Infrared Spectroscopy

REFERENCES

1. P. Patimisco, A. Sampaolo, F.K. Tittel, V. Spagnolo, ‘Mode Matching of a Laser-Beam to a Compact High Finesse Bow-Tie Optical Cavity for Quartz Enhanced Photoacoustic Gas Sensing’, *Sens. Actuator A Phys.*, **267**, 70 (2017).
2. M. Slatkine, ‘Ultimate Sensitivity of Liquid Optoacoustic Spectroscopy Using Chopped cw Lasers’, *Appl. Opt.*, **20**, 2880 (1981).
3. V.P. Zharov, V.S. Letokhov, *Laser Optoacoustic Spectroscopy*, Springer Berlin, Berlin, Vol. 37, 1986.
4. V. Spagnolo, P. Patimisco, S. Borri, G. Scamarcio, B.E. Bernacki, J.M. Kriesel, ‘Part-Per-Trillion Level SF6 Detection Using a Quartz Enhanced Photoacoustic Spectroscopy Based Sensor with Single-Mode Fiber-Coupled Quantum Cascade Laser Excitation’, *Opt. Lett.*, **37**, 460 (2012).
5. T. Tomberg, M. Vainio, T. Hieta, L. Halonen, ‘Sub-Parts-Per-Trillion Level Sensitivity in Trace Gas Detection by Cantilever-Enhanced Photo-Acoustic Spectroscopy’, *Sci. Rep.*, **8**, 1848 (2018).
6. M. Viengerov, ‘New Method of Gas Analysis Based on Tyndall-Roentgen Opto-Acoustic Effect’, *Dokl. Akad. Nauk SSSR*, **19**, 687 (1938).
7. E.L. Kerr, J.G. Atwood, ‘The Laser Illuminated Absorptivity Spectrophone: A Method for Measurement of Weak Absorptivity in Gases at Laser Wavelengths’, *Appl. Opt.*, **7**, 915 (1968).
8. L.B. Kreuzer, N.D. Kenyon, C.K.N. Patel, ‘Air Pollution: Sensitive Detection of Ten Pollutant Gases by Carbon Monoxide and Carbon Dioxide Lasers’, *Science*, **177**, 347 (1972).
9. E. Max, L. Rosengren, ‘Characteristics of a Resonant Opto-Acoustic Gas Concentration Detector’, *Opt. Commun.*, **11**, 422 (1974).
10. S. Manohar, D. Razansky, ‘Photoacoustics: A Historical Review’, *Adv. Opt. Photonics*, **8**, 586 (2016).
11. L.B. Kreuzer, ‘Ultralow Gas Concentration Infrared Absorption Spectroscopy’, *J. Appl. Phys.*, **42**, 2934 (1971).
12. S.E. Bialkowski, N.G.C. Astrath, M.A. Proskurnin, *Photothermal Spectroscopy Methods*, John Wiley & Sons, Hoboken, NJ, 2019.
13. B.J. Berne, R. Pecora, *Dynamic Light Scattering*, John Wiley & Sons, New York, 1976.
14. P. Patimisco, G. Scamarcio, F.K. Tittel, V. Spagnolo, ‘Quartz-Enhanced Photoacoustic Spectroscopy: A Review’, *Sensors*, **14**, 6165 (2014).
15. P. Patimisco, A. Sampaolo, L. Dong, F.K. Tittel, V. Spagnolo, ‘Recent Advances in Quartz Enhanced Photoacoustic Sensing’, *Appl. Phys. Rev.*, **5**, 011106 (2018).
16. P. Patimisco, A. Sampaolo, Y. Bidaux, A. Bismuto, M. Schott, J. Jiang, A. Muller, J. Faist, F.K. Tittel, V. Spagnolo, ‘Purely Wavelength- and Amplitude-Modulated Quartz-Enhanced Photoacoustic Spectroscopy’, *Opt. Express*, **24**, 25943 (2016).
17. A.A. Kosterev, Y.A. Bakhirkin, R.F. Curl, F.K. Tittel, ‘Quartz-Enhanced Photoacoustic Spectroscopy’, *Opt. Lett.*, **27**, 1902 (2002).
18. A.A. Kosterev, F.K. Tittel, D. Serebryakov, A. Malinovsky, A. Morozov, ‘Applications of Quartz Tuning Fork in

Spectroscopic Gas Sensing', *Rev. Sci. Instrum.*, **76**, 043105 (2005).

19. P. Patimisco, A. Sampaolo, M. Giglio, V. Mackoviak, H. Rossmadl, B. Gross, A. Cable, F.K. Tittel, V. Spagnolo, 'Octupole Electrode Pattern for Tuning Forks Vibrating at the First Overtone Mode in Quartz-Enhanced Photoacoustic Spectroscopy', *Opt. Lett.*, **43**, 1854 (2018).
20. W.H. Flygare, 'Molecular Relaxation', *Acc. Chem. Res.*, **1**, 121 (1968).
21. V. Spagnolo, A.A. Kosterev, L. Dong, R. Lewicki, F.K. Tittel, 'NO Trace Gas Sensor Based on Quartz-Enhanced Photoacoustic Spectroscopy and External Cavity Quantum Cascade Laser', *Appl. Phys. B*, **100**, 125 (2010).
22. L. Dong, V. Spagnolo, R. Lewicki, F.K. Tittel, 'Ppb-Level Detection of Nitric Oxide Using an External Cavity Quantum Cascade Laser Based QEPAS Sensor', *Opt. Express*, **19**, 24037 (2011).
23. P. Patimisco, A. Sampaolo, M. Giglio, S. Dello Russo, V. Mackowiak, H. Rossmadl, A. Cable, F.K. Tittel, V. Spagnolo, 'Tuning Forks With Optimized Geometries for Quartz-Enhanced Photoacoustic Spectroscopy', *Opt. Express*, **27**, 1401 (2019).
24. P. Patimisco, S. Borri, A. Sampaolo, H.E. Beere, D.A. Ritchie, M.S. Vitiello, G. Scamarcio, V. Spagnolo, 'Quartz Enhanced Photo-Acoustic Gas Sensor Based on Custom Tuning Fork and Terahertz Quantum Cascade Laser', *Analyst*, **139**, 2079 (2014).
25. F.K. Tittel, A. Sampaolo, P. Patimisco, L. Dong, A. Geras, T. Starecki, V. Spagnolo, 'Analysis of Overtone Flexural Modes Operation in Quartz-Enhanced Photoacoustic Spectroscopy', *Opt. Express*, **24**, A682 (2016).
26. H. Hosaka, K. Itao, S. Kuroda, 'Damping Characteristics of Beam-Shaped Micro-oscillators', *Sens. Actuator A Phys.*, **49**, 87 (1995).
27. Z. Hao, A. Erbil, F. Ayazi, 'An Analytical Model for Support Loss in Micromachined Beam Resonators With in-Plane Flexural Vibrations', *Sens. Actuator A Phys.*, **109**, 156 (2003).
28. C. Zener, 'Internal Friction in Solids II. General Theory of Thermoelastic Internal Friction', *Phys. Rev.*, **53**, 90 (1938).
29. M. Giglio, G. Menduni, P. Patimisco, A. Sampaolo, A. Elefante, V.M.N. Passaro, V. Spagnolo, 'Damping Mechanisms of Piezoelectric Quartz Tuning Forks Employed in Photoacoustic Spectroscopy for Trace Gas Sensing', *Phys. Status Solidi A*, **216**, 1800552 (2019).
30. P. Patimisco, A. Sampaolo, V. Mackowiak, H. Rossmadl, A. Cable, F.K. Tittel, V. Spagnolo, 'Loss Mechanisms Determining the Quality Factors in Quartz Tuning Forks Vibrating at the Fundamental and First Overtone Modes', *IEEE T. Ultrason. Ferr.*, **65**, 1951 (2018).
31. W.K. Blake, 'The Radiation From Free-Free Beams in Air and in Water', *J. Sound Vib.*, **33**, 427 (1974).
32. S. Li, L. Dong, H. Wu, A. Sampaolo, P. Patimisco, V. Spagnolo, F.K. Tittel, 'Ppb-Level Quartz-Enhanced Photoacoustic Detection of Carbon Monoxide Exploiting a Surface Grooved Tuning Fork', *Anal. Chem.*, **91**, 5834 (2019).
33. F. Sgobba, G. Menduni, S. Dello Russo, A. Sampaolo, P. Patimisco, M. Giglio, E. Ranieri, V.M.N. Passaro, F.K. Tittel, V. Spagnolo, 'Quartz-Enhanced Photoacoustic Detection of Ethane in the Near-IR Exploiting a Highly Performant Spectrophone', *Appl. Sci.*, **10**, 2447 (2020).
34. Y. Ma, Y. He, P. Patimisco, A. Sampaolo, S. Qiao, X. Yu, F.K. Tittel, V. Spagnolo, 'Ultra-High Sensitive Trace Gas Detection Based on Light-Induced Thermoelastic Spectroscopy and a Custom Quartz Tuning Fork', *Appl. Phys. Lett.*, **116**, 011103 (2020).
35. S. Li, H. Wu, R. Cui, A. Sampaolo, P. Patimisco, V. Spagnolo, F.K. Tittel, L. Dong, 'Piezo-Enhanced Acoustic Detection Module for Mid-Infrared Trace Gas Sensing Using a Grooved Quartz Tuning Fork', *Opt. Express*, **27**, 35267 (2019).
36. K. Liu, X. Guo, H. Yi, W. Chen, W. Zhang, X. Gao, 'Off-Beam Quartz-Enhanced Photoacoustic Spectroscopy', *Opt. Lett.*, **34**, 1594 (2009).
37. S. Böttger, M. Köhring, U. Willer, W. Schade, 'Off-Beam Quartz-Enhanced Photoacoustic Spectroscopy with LEDs', *Appl. Phys. B Lasers Opt.*, **113**, 227 (2013).
38. S. Dello Russo, M. Giglio, A. Sampaolo, P. Patimisco, G. Menduni, H. Wu, L. Dong, V.M.N. Passaro, V. Spagnolo, 'Acoustic Coupling between Resonator Tubes in Quartz-Enhanced Photoacoustic Spectrophones Employing a Large Prong Spacing Tuning Fork', *Sensors*, **19**, 4109 (2019).
39. N. Ogawa, F. Kaneko, 'Open End Correction for a Flanged Circular Tube Using the Diffusion Process', *Eur. J. Phys.*, **34**, 1159 (2013).
40. A. Sampaolo, P. Patimisco, L. Dong, A. Geras, G. Scamarcio, T. Starecki, F.K. Tittel, V. Spagnolo, 'Quartz-Enhanced Photoacoustic Spectroscopy Exploiting Tuning Fork Overtone Modes', *Appl. Phys. Lett.*, **107**, 231102 (2015).
41. H. Zheng, L. Dong, P. Patimisco, H. Wu, A. Sampaolo, X. Yin, S. Li, W. Ma, L. Zhang, W. Yin, L. Xiao, V. Spagnolo, S. Jia, F.K. Tittel, 'Double Antinode Excited Quartz-Enhanced Photoacoustic Spectrophone', *Appl. Phys. Lett.*, **110**, 021110 (2017).
42. H. Wu, X. Yin, L. Dong, K. Pei, A. Sampaolo, P. Patimisco, H. Zheng, W. Ma, L. Zhang, W. Yin, L. Xiao, V. Spagnolo, S. Jia, F.K. Tittel, 'Simultaneous Dual-Gas QEPAS Detection Based on a Fundamental and Overtone Combined Vibration of Quartz Tuning Fork', *Appl. Phys. Lett.*, **110**, 121104 (2017).

---

43. A. Elefante, M. Giglio, A. Sampaolo, G. Menduni, P. Patimisco, V.M.N. Passaro, H. Wu, H. Rossmadl, V. Mackowiak, A. Cable, F.K. Tittel, L. Dong, V. Spagnolo, 'Dual-Gas Quartz-Enhanced Photoacoustic Sensor for Simultaneous Detection of Methane/Nitrous Oxide and Water Vapor', *Anal. Chem.*, **91**, 12866 (2019).
44. F.J.M. Harren, S.M. Cristescu, 'Photoacoustic Spectroscopy in Trace Gas Monitoring', in *Encyclopedia of Analytical Chemistry*, John Wiley & Sons, Ltd., Hoboken, NJ, 2000.
45. M. Jahjah, W. Kiang, N.P. Sanchez, W. Ren, P. Patimisco, V. Spagnolo, S.C. Herndon, R.J. Griffin, F.K. Tittel, 'Atmospheric CH_4 and N_2O Measurements Near Greater Houston Area Landfills Using QCL-Based QEPAS Sensor System During DISCOVERY-AQ 2013', *Opt. Lett.*, **39**, 957 (2014).
46. H. Wu, L. Dong, X. Yin, A. Sampaolo, P. Patimisco, W. Ma, L. Zhang, W. Yin, L. Xiao, V. Spagnolo, S. Jia, 'Atmospheric CH_4 Measurement Near a Landfill Using an ICL-Based QEPAS Sensor with V-T Relaxation Self-Calibration', *Sens. Actuators B Chem.*, **297**, 126753 (2019).
47. A. Elefante, G. Menduni, H. Rossmadl, V. Mackowiak, M. Giglio, A. Sampaolo, P. Patimisco, V.M.N. Passaro, V. Spagnolo, 'Environmental Monitoring of Methane with Quartz-Enhanced Photoacoustic Spectroscopy Exploiting an Electronic Hygrometer to Compensate the H_2O Influence on the Sensor Signal', *Sensors*, **20**, 2935 (2020).
48. M. Giglio, A. Zifarelli, A. Sampaolo, G. Menduni, A. Elefante, R. Blanchard, C. Pfluegl, M.F. Witinski, D. Vakhshoori, H. Wu, V.M.N. Passaro, P. Patimisco, F.K. Tittel, L. Dong, V. Spagnolo, 'Broadband Detection of Methane and Nitrous Oxide Using a Distributed Feedback Quantum Cascade Laser Array and Quartz-Enhanced Photoacoustic Sensing', *Photoacoustics*, **17**, 100159 (2020).
49. S. Zhou, L. Xu, L. Zhang, T. He, N. Liu, Y. Liu, B. Yu, J. Li, 'External Cavity Quantum Cascade Laser-Based QEPAS for Chlorodifluoromethane Spectroscopy and Sensing', *Appl. Phys. B*, **125**, 125 (2019).
50. A. Sampaolo, S. Csutak, P. Patimisco, M. Giglio, G. Menduni, V. Passaro, F.K. Tittel, M. Deffenbaugh, V. Spagnolo, 'Methane, Ethane and Propane Detection Using a Compact Quartz Enhanced Photoacoustic Sensors and a Single Interband Cascade Laser', *Sens. Actuators B Chem.*, **282**, 952 (2019).
51. A. Sampaolo, G. Menduni, P. Patimisco, M. Giglio, V.M.N. Passaro, L. Dong, H. Wu, F.K. Tittel, V. Spagnolo, 'Quartz-Enhanced Photoacoustic Spectroscopy for Hydrocarbon Trace Gas Detection and Petroleum Exploration', *Fuel*, **227**, 112112 (2020).
52. A. Sampaolo, P. Patimisco, M. Giglio, L. Chieco, G. Scamarcio, F.K. Tittel, V. Spagnolo, 'Highly Sensitive Gas Leak Detector Based on a Quartz-Enhanced Photoacoustic SF_6 Sensor', *Opt. Express*, **24**, 15872 (2016).
53. M. Maiss, C.A.M. Brenninkmeijer, 'Atmospheric SF_6: Trends, Sources, and Prospects', *Environ. Sci. Technol.*, **32**, 3077 (1998).
54. C. Shi, D. Wang, Z. Wang, L. Ma, Q. Wang, K. Xu, S.-C. Chen, W. Ren, 'A Mid-Infrared Fiber-Coupled QEPAS Nitric Oxide Sensor for Real-Time Engine Exhaust Monitoring', *IEEE Sens. J.*, **17**, 7418 (2017).
55. C. Wang, P. Sahay, 'Breath Analysis Using Laser Spectroscopic Techniques: Breath Biomarkers, Spectral Fingerprints, and Detection Limits', *Sensors*, **9**, 8230 (2009).
56. K.H. Kim, S.A. Jahan, E. Kabir, 'A Review of Breath Analysis for Diagnosis of Human Health', *Anal. Chem.*, **33**, 1 (2018).
57. S. Davies, P. Spanel, D. Smith, 'Quantitative Analysis of Ammonia on the Breath of Patients in End-Stage Renal Failure', *Kidney Int.*, **52**, 223 (1997).
58. M.R. McCurdy, A. Sharafkhaneh, H. Abdel-Monem, J. Rojo, F.K. Tittel, 'Exhaled Nitric Oxide Parameters and Functional Capacity in Chronic Obstructive Pulmonary Disease', *J. Breath Res.*, **5**, 016003 (2011).
59. M. Giglio, A. Elefante, P. Patimisco, A. Sampaolo, F. Sgobba, H. Rossmadl, V. Mackowiak, H. Wu, F.K. Tittel, L. Dong, V. Spagnolo, 'Quartz-Enhanced Photoacoustic Sensor for Ethylene Detection Implementing Optimized Custom Tuning Fork-Based Spectrophone', *Opt. Express*, **27**, 4271 (2019).
60. J.P. Waclawek, H. Moser, B. Lendl, 'Compact Quantum Cascade Laser Based Quartz-Enhanced Photoacoustic Spectroscopy Sensor System for Detection of Carbon Disulfide', *Opt. Express*, **24**, 6559 (2016).
61. S.F. Solga, M. Mudalel, L.A. Spacek, R. Lewicki, F.K. Tittel, C. Loccioni, A. Russo, T.H. Risby, 'Factors Influencing Breath Ammonia Determination', *J. Breath Res.*, **7**, 037101 (2013).
62. N. Maurin, R. Rousseau, W. Trzpil, G. Aoust, M. Hayot, J. Mercier, M. Bahriz, F. Gouzi, A. Vicet, 'First Clinical Evaluation of a Quartz Enhanced Photo-Acoustic CO Sensor for Human Breath Analysis', *Sens. Actuators B Chem.*, **319**, 128247 (2020).
63. A. Zifarelli, M. Giglio, G. Menduni, A. Sampaolo, P. Patimisco, V.M.N. Passaro, H. Wu, L. Dong, V. Spagnolo, 'Partial Least-Squares Regression as a Tool to Retrieve Gas Concentrations in Mixtures Detected Using Quartz-Enhanced Photoacoustic Spectroscopy', *Anal. Chem.*, **92**, 11035 (2020).

This article was published in the *Encyclopedia of Analytical Chemistry* in 2021 by John Wiley & Sons, Ltd.
DOI: 10.1002/9780470027318.a9760